ROYAL SOCIETY OF CHEMISTRY

## PAPER

Check for updates

# Supramolecular assemblies and nanoparticle integration studied through quantitative image analysis and 3D reconstruction

Daeun Jeong,†[a,b] Hyoung Wook Kang,†[a,b] Seojeong Woo,†[a,b] Semi Kim,[a,b] Soo Ryeon Yoon,[a,b] Jaedeok Lee,[a,b] Cheongwon Bae,[a,b] Ho-Jun Cho,[a,b] Mingyu Gu,[a,b] Jong Hwa Jung, [iD] [a,b] Ju Hyun Kim,[c] Kwang Seob Jeong, [iD] [d] Sung Ho Jung [iD] *[a,b] and Juyeong Kim [iD] *[a,b]

Nanoparticle incorporation into supramolecular assemblies is essential for designing hybrid nanostructures with tailored optical and structural properties. However, understanding the interactions that govern the attachment and formation of such composites remains a challenge, particularly when complex structures are involved. In this study, we explore the fabrication of quantum dot (QD)/ J-aggregate composites of tetrakis(4-sulfonatophenyl)porphyrin ($H_2TPPS_4$), where electrostatic interactions between cysteamine-functionalized QDs and negatively charged J-aggregates of $H_4TPPS_4$ with L-alanine play a key role in their formation. By systematically varying QD concentration, we examine how QD loading influences the structure and attachment pattern of the composites. Quantitative transmission electron microscopy (TEM) image analysis and three-dimensional (3D) TEM tomography were employed to obtain detailed insights into the interparticle spacing, thickness distribution, and 3D morphology of the QD/J-aggregate composites. The results show that higher QD concentrations lead to multilayered structures with decreased interparticle spacing, and TEM tomography reveals the helical arrangement of QDs on the framework of $H_4TPPS_4$ with L-alanine. This work emphasizes the critical role of advanced imaging techniques and quantitative analyses in understanding the evolution of nanoparticle assemblies, opening new possibilities for the design of advanced hybrid nanostructures.

## Introduction

Supramolecular self-assemblies, formed through non-covalent interactions such as hydrogen bonding, π–π stacking, and van der Waals forces, offer tunable architectures with various applications in nanotechnology, catalysis, and materials science.[1–6] Their dynamic and reversible nature allows for precise functionalization and adaptability to external stimuli,[7–11] distinguishing them from conventional nanomaterials. The ability to integrate functional nanoparticles (NPs) into these self-assemblies leads to the formation of hybrid materials that exhibit enhanced stability, electronic properties, and reactivity.[12–19] This synergy improves charge trans-

port, energy transfer, and catalytic efficiency, positioning supramolecular assemblies as promising candidates for advanced biofunctional applications.[20] However, precise control and characterization of NP adsorption within supramolecular matrices remains a challenge due to variations in interfacial interactions and aggregation tendency. This challenge necessitates detailed structural characterization and a deeper understanding of the spatial distribution and interfacial interactions within these hybrid systems.

Recent advances have demonstrated the potential of porphyrin-based supramolecular structures in hybrid materials, particularly due to their defined coordination chemistry, redox activity, and tunable optical properties.[21–33] For example, porphyrin assemblies have been shown to form mirror-image helical nanorods in the presence of chiral species in organic media.[34] One study reported that a chiral amphiphilic histidine directed the self-assembly of a carboxylic acid-functionalized porphyrin into hierarchical chiral microstructures, whose superhydrophobic surfaces enabled macroscopic enantioselective recognition of amino acids.[35] Despite these promising developments, a key obstacle is the difficulty in achieving

[a]*Department of Chemistry, Gyeongsang National University, Jinju 52828, South Korea. E-mail: shjung@gnu.ac.kr*
[b]*Research Institute of Advanced Chemistry, Gyeongsang National University, Jinju 52828, South Korea. E-mail: chris@gnu.ac.kr*
[c]*Department of Chemistry, Dongguk University, Seoul 04620, South Korea*
[d]*Department of Chemistry, Korea University, Seoul 02841, South Korea*
† Equal contribution.

consistent and stable NP adsorption within supramolecular frameworks, which often leads to undesired aggregation or uneven distribution.

In this study, we investigate the adsorption behavior and structural organization of quantum dots (QDs) within tetrakis(4-sulfonatophenyl)porphyrin ($H_2TPPS_4$) assemblies. By employing advanced image analysis and three-dimensional (3D) morphological reconstruction, we quantitatively characterize the spatial distribution of QDs on supramolecular structures. Our findings offer valuable insights into the design of inorganic–organic supramolecular hybrid materials, particularly for applications in optoelectronics and energy conversion.

# Results and discussion

The J-aggregates of $H_4TPPS_4$ were prepared by adding chiral L-alanine in a solution of monomeric $H_2TPPS_4$ (Fig. 1), which induces electrostatic interactions between the anionic sulfonate groups and positively charged porphyrin rings.[36] The characteristic features of J-aggregates of $H_4TPPS_4$ with L-alanine were observed in the UV-vis absorption spectrum, displaying a red-shifted Soret band at 487 nm and a blue-shifted band at 420 nm compared to the monomeric $H_2TPPS_4$ (Fig. S1, SI).[37] Furthermore, the chirality of the L-alanine was transferred to the porphyrin assemblies, resulting in a pronounced Cotton effect in the circular dichroism (CD) spectrum. The Cotton effect, which arises from the differential absorption of left- and right-circularly polarized light, is a key indicator of chiral induction in supramolecular systems.[38–41] The CD measurements revealed a first negative CD signal at 493 nm in the Soret band region caused by the addition of L-alanine, which contributed to inducing left-handed helicity in the supramolecular assemblies (Fig. S2, SI).

CdSe/ZnS core–shell QDs were synthesized via a two-step colloidal method (see details in the SI).[42] CdSe cores were prepared using the hot-injection method. A cadmium precursor solution was prepared by dissolving CdO and $Zn(CH_3COO)_2$ in oleic acid under vacuum at 150 °C, followed by the addition of 1-octadecene under a $N_2$ atmosphere. The temperature was increased to 320 °C, and a selenium precursor solution including tri-*n*-octylphosphine and Se/S was rapidly injected, initiating nucleation and growth. The reaction was maintained at 300 °C for 10 minutes, followed by rapid cooling at a rate of approximately 55 °C min$^{-1}$ to 80 °C. The ZnS shell was subsequently grown via successive ion layer adsorption and reaction to passivate surface defects.

The original hydrophobic and neutral surface ligand on the QDs, tri-*n*-octylphosphine oxide, was exchanged for a hydrophilic and positively charged ligand, cysteamine, to enhance solvent compatibility with the J-aggregates of $H_4TPPS_4$ and enable electrostatic interactions (Fig. 2a). Despite the change in surface functionality, no significant changes were observed in the photoluminescence (PL) properties at 482 nm before and after ligand exchange (Fig. 2b), suggesting that the ligand modification had minimal impact on the optical characteristics of the QDs. The QDs had an absorption edge around 500 nm in the UV-vis absorption spectrum (Fig. S3).

The QD solution was then combined with the assemblies of chiral J-aggregates, followed by mild shaking, yielding QD/ J-aggregate composites (Fig. 1 and S4, SI). Since the QDs were functionalized via ligand exchange with cysteamine, imparting a positive surface charge, electrostatic attraction between the negatively charged surface of J-aggregates and the positively charged QDs facilitated the formation of stable QD/J-aggregate composites. In addition, the composites remained colloidally
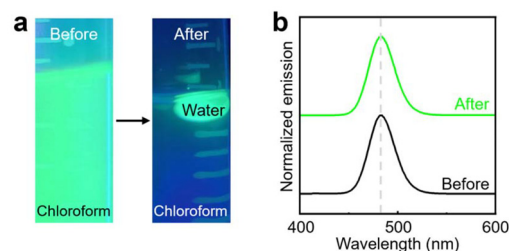


**Fig. 2** (a) Photographs of the QD solution before and after surface ligand exchange from tri-*n*-octylphosphine to cysteamine. (b) PL spectra of tri-*n*-octylphosphine-modified QDs (black) and cysteamine-modified QDs (green).
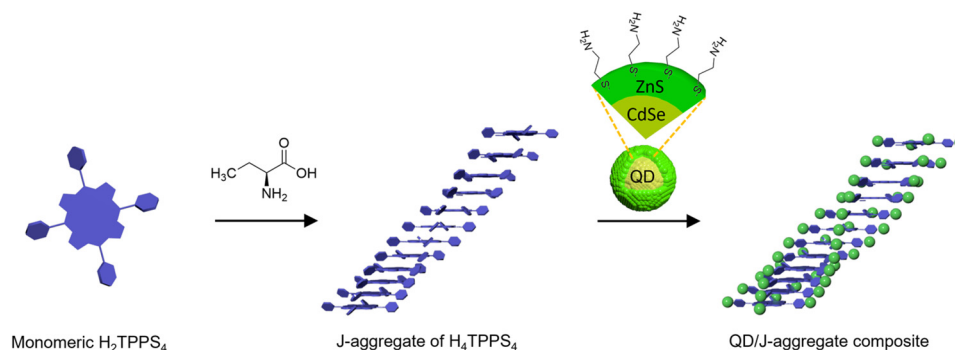


**Fig. 1** Schematic representation of the QD/J-aggregate composite formation.

stable under our experimental conditions, although gradual dissociation was observed over two months (Fig. S5, SI). As a property of the J-aggregates, their characteristic absorption features diminished upon heating to 80 °C, accompanied by the emergence of a monomeric porphyrin band.

Transmission electron microscopy (TEM) analysis confirmed that the QDs maintained a uniform size distribution with an average diameter of 15.1 ± 1.1 nm (Fig. 3a and b). Supramolecular assemblies formed with $H_4TPPS_4$ in the presence of L-alanine were observed as long and thin nanowire-like structures with an average thickness of 51.7 ± 15.0 nm (Fig. 3c and d). QD/J-aggregate composite structures are shown, where QDs are densely attached to the surface of the J-aggregates with variations in composite's thickness (Fig. 3e).

To verify the presence of QDs on the J-aggregates, TEM elemental mapping was performed (Fig. 3f). Distinct QD signals were observed across the J-aggregates, and elemental analysis of the QD-bound regions revealed the characteristic signals of Cd, Zn, and S. These results confirm the successful integration of QDs into the supramolecular assembly, resulting in a hybrid nanostructure.

Spectroscopic analysis was performed to understand the optical properties of QD/J-aggregate composites. Upon incorporation of the QDs, the UV-vis absorption spectrum of the

QD/J-aggregate composites closely resembled that of the J-aggregates (Fig. 4a), with increased absorbance around 420 nm and 487 nm, likely due to the influence of the QDs. In addition, CD spectroscopy confirmed that the QD/J-aggregate composites adopted a helical conformation (Fig. 4b), displaying left-handed helicity in their respective CD signal. This observation implies that the chirality of J-aggregates transferred to QDs *via* electrostatic interactions of QD/J-aggregate composites. PL measurements showed that the J-aggregates displayed four characteristic emission peaks at 470, 500, 670, and 720 nm (Fig. S6, SI). The QD/J-aggregate composites retained a similar PL peak pattern to the J-aggregates. While spectral overlap suggests potential energy transfer between QDs and J-aggregates, the dominant emission from the J-aggregates obscured QD contributions, limiting clear interpretation.

We investigated the effect of QD concentration on the formation of QD/J-aggregate composites and monitored structural changes through quantitative image analysis. The volume fraction of QDs was varied from 0.02 to 0.5 vol% relative to the total solution volume including the J-aggregate solution (Fig. 5a), while maintaining the J-aggregate conditions constant. TEM images showed that at lower QD concentrations, fewer QDs were attached to the J-aggregate surface. In contrast, at higher QD concentrations, QDs were not only bound to the J-aggregate structures but also accumulated on pre-attached QDs, leading to the formation of multilayered QD/J-aggregate composites.

To obtain a quantitative relationship between the QD concentration and the attachment pattern, image analysis was conducted using ImageJ and our customized MATLAB code to determine the thickness distribution of QD/J-aggregate composites and the interparticle spacing between attached QDs (Fig. 5b, c and S7–S11, SI).[43] At a low QD concentration of 0.02 vol%, the thickness distribution of the QD/J-aggregate composites was broad. As the QDs increasingly enveloped the J-aggregates, the distribution converged, indicating a more uniform strand thickness. However, at a high QD concentration of 0.5 vol%, the distribution broadened again, likely due to the helical arrangement of QDs along the framework of H4TPPS4 with L-alanine. The extent of thickness fluctuations increased with QD concentration, further supporting the formation of multilayered QD assemblies. In addition, the average thickness of QD/J-aggregate composites showed a concentration-dependent trend: 55.2 ± 22.5 nm at 0.1 vol%, 76.1 ±
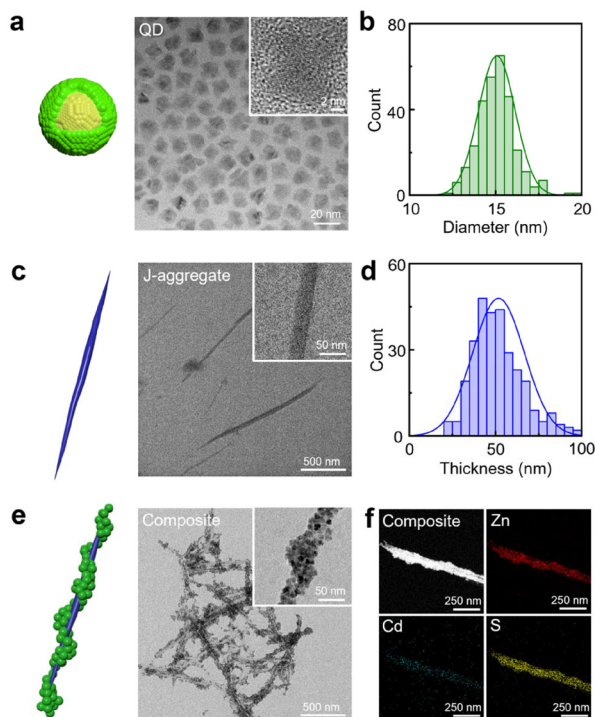


**Fig. 3** (a) Representative TEM images of QDs. (b) Diameter distribution histogram for QDs. (c) Representative TEM images of J-aggregates of $H_4TPPS_4$. (d) Thickness distribution histogram for J-aggregates of $H_4TPPS_4$. (e) Representative TEM images of QD/J-aggregate composites. (f) TEM elemental mapping of QD/J-aggregate composites (red: Zn, cyan: Cd, and yellow: S). Each histogram in (b) and (d) was generated based on 300 individual measurements.
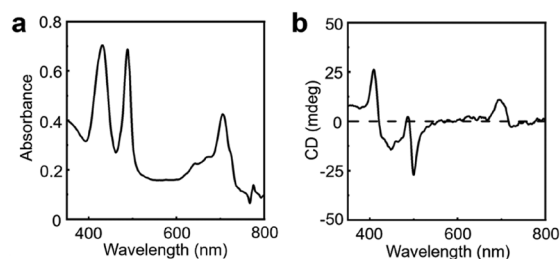


**Fig. 4** (a) UV-vis absorption spectrum of QD/J-aggregate composites. (b) CD spectrum of QD/J-aggregate composites.
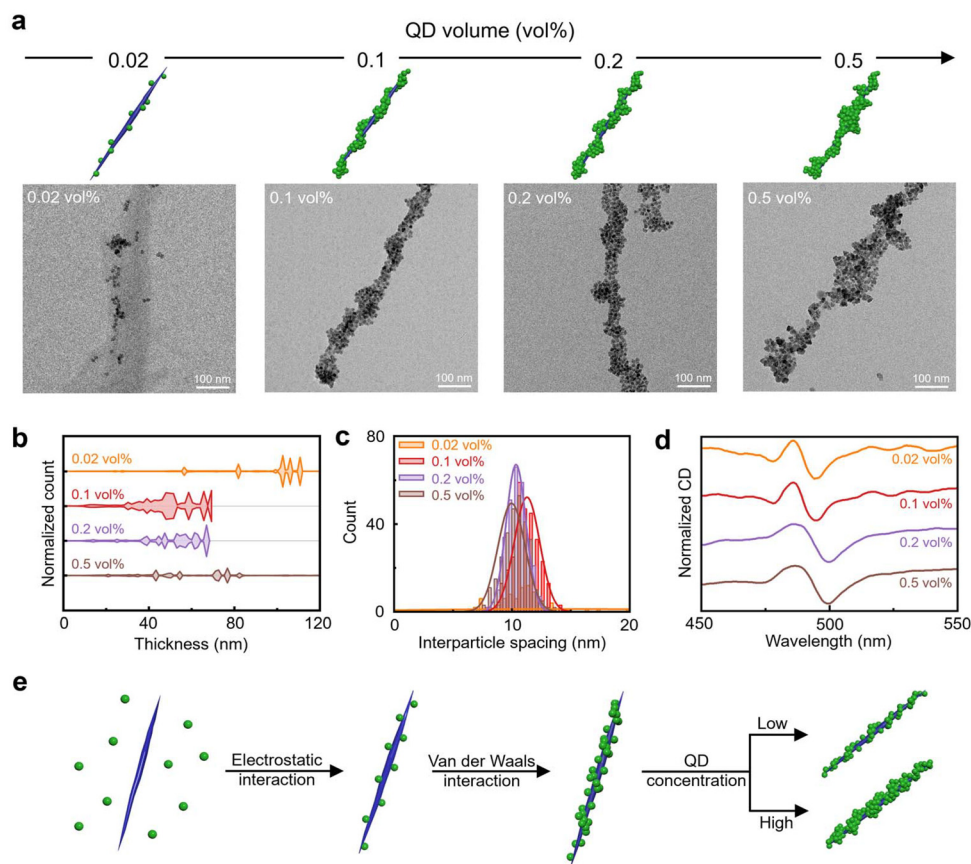
**Fig. 5** (a) Representative illustrations and the corresponding TEM images of QD/J-aggregate composites synthesized with different QD concentrations (from left to right: 0.02, 0.1, 0.2, and 0.5 vol%). (b) Thickness distribution histograms for QD/J-aggregate composites at different QD concentrations (brown: 0.02 vol%, red: 0.1 vol%, light red: 0.2 vol%, and pale red: 0.5 vol%). (c) Interparticle spacing distribution histograms for QD/J-aggregate composites at different QD concentrations. (d) Normalized CD spectra of QD/J-aggregate composites at different QD concentrations. (e) Schematic of the QD attachment process to J-aggregates.

30.4 nm at 0.2 vol%, and 77.4 ± 35.7 nm at 0.5 vol%. This gradual increase in thickness suggests a transition from monolayer to multilayer QD attachment on the J-aggregates. It is noted that at 0.02 vol%, several assembly strands tended to bundle together (average thickness = 73.8 ± 30.8 nm), which appears to be independent of QD attachment.

The effect of QD concentration on the interparticle spacing between QDs attached to the J-aggregates was also investigated (Fig. 5c). As the QD concentration increased, the average spacing between QDs gradually decreased (14.1 nm at 0.02 vol%, 11.2 nm at 0.1 vol%, 9.6 nm at 0.2 vol%, and 9.4 nm at 0.5 vol%). However, the extent of this decrease showed only weak dependence on QD concentration. Notably, at 0.02 vol%, QDs tended to cluster together on the J-aggregates rather than being individually dispersed. This behavior implies that the initially attached QDs acted as nucleation sites, facilitating the subsequent attachment of additional QDs in close proximity. These findings highlight the combined influence of electrostatic interactions between QDs and J-aggregates and van der Waals forces among QDs themselves in governing QD/J-aggregate composite formation. It is noted that distinguishing overlapping QDs in 3D space is challenging because our

analysis was based on 2D TEM images. The measured interparticle distances reflect only those QDs that appeared spatially separated within the 2D projection.

The CD spectra of the QD/J-aggregate composites were analyzed as a function of QD concentration (Fig. 5d). All spectra exhibited left-handed chirality, in agreement with the helical nature of the J-aggregates. At higher QD concentrations (0.2 vol% and 0.5 vol%), the negative signal around 500 nm was red shifted compared to those observed at lower concentrations. These peak shifts may result from structural distortions in the $H_4TPPS_4$ building blocks induced by the increased QD loading. Furthermore, the positive band in the CD spectra broadened with increasing QD concentration, particularly in the composites prepared with 0.2 vol% and 0.5 vol% QDs. This broadening is likely associated with greater variability in QD attachment, which may become more pronounced at higher QD concentrations.

The mechanism of QD attachment and composite formation on J-aggregates is summarized as follows (Fig. 5e). At lower QD concentrations, individual QDs attach to the J-aggregate surface, acting as nucleation sites for further QD accumulation. This process is primarily driven by electrostatic
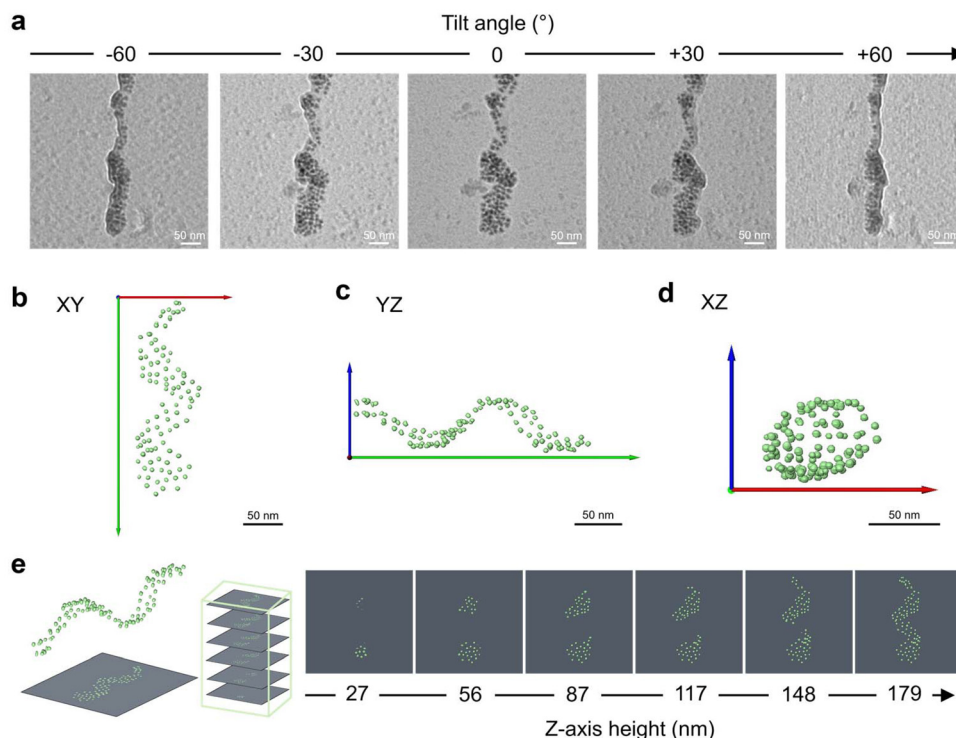
**Fig. 6** (a) TEM images of the QD/J-aggregate composite captured at various tilt angles. (b–d) 3D reconstruction images of the QD/J-aggregate composite viewed from different perspectives. (e) Accumulated Z-slices of the reconstructed tomograms of the QD/J-aggregate composite.

interactions between the QDs and the J-aggregates, as well as van der Waals forces among the QDs. As the QD concentration increases, additional QDs not only bind to the J-aggregate surface but also accumulate on pre-attached QDs, forming multilayered composites. This enhanced accumulation leads to increased structural complexity and thickness, while also inducing distortions in the J-aggregates due to the higher QD loading.

We further examined the 3D morphology of the QD/J-aggregate composites using TEM tomography (Fig. 6), as the intricate QD attachment pattern on the J-aggregate could not be clearly visualized in conventional 2D TEM images. A series of tilt TEM images were acquired for a single composite over the −60° to +60° tilt range in 2° increments (Fig. 6a and Movie S1, SI). The 3D reconstruction of the QD/J-aggregate composite confirmed the uniform distribution of QDs on the J-aggregate surface (Fig. 6b–d and Movie S2, SI) and distinctly revealed their left-handed helical arrangement. Moreover, cross-sectional images obtained along the Z-axis demonstrated that QDs were partially assembled in a multilayered structure (Fig. 6e and Movie S3, SI). These results indicate that the formation of QD domains is influenced by the structural arrangement and inherent helicity of the J-aggregates.

mine-functionalized QDs and negatively charged $H_4TPPS_4$ with L-alanine assemblies. By systematically varying the QD concentration, we observed that higher QD concentrations led to the formation of multilayered composite structures, accompanied by increased thickness and a more complex attachment pattern. Quantitative image analysis revealed that the interparticle spacing decreased as the QD concentration increased. Furthermore, CD spectroscopy confirmed the preservation of left-handed helicity in both the J-aggregate assemblies and the QD/J-aggregate composites, with subtle optical changes due to increased QD loading with chirality transfer. TEM tomography was employed to gain deeper insight into the 3D morphology of the composites, showing the helical arrangement of QDs on the framework of H4TPPS4 with L-alanine. The results highlight the role of both electrostatic interactions and van der Waals forces in driving QD attachment, and demonstrate how the structural arrangement and inherent helicity of the $H_4TPPS_4$ assemblies influence the formation of QD domains. These findings pave the way for the development of hybrid nanostructures with tailored optical and structural properties for potential applications in nanotechnology and materials science.

## Conclusions

In this study, we successfully fabricated QD/J-aggregate composites by exploiting electrostatic interactions between cystea-

## Author contributions

Conceptualization, S. H. J. and J. K.; validation, D. J., H. W. K., S. W., J. H. J., S. H. J., and J. K.; formal analysis, D. J., H. W. K.,

## Conflicts of interest

There are no conflicts to declare.

## Data availability

The data supporting this article have been included as part of the SI.

Image analysis and the corresponding MATLAB code are provided in Section 4 of the SI. See DOI: https://doi.org/10.1039/d5dt01505g.

## Acknowledgements

## References

1 C. Li, M. Numata, A.-H. Bae, K. Sakurai and S. Shinkai, Self-assembly of supramolecular chiral insulated molecular wire, *J. Am. Chem. Soc.*, 2005, **127**, 4548–4549.

2 T. F. A. De Greef, M. M. J. Smulders, M. Wolffs, A. P. H. J. Schenning, R. P. Sijbesma and E. W. Meijer, Supramolecular polymerization, *Chem. Rev.*, 2009, **109**, 5687–5754.

3 T. Aida, E. W. Meijer and S. I. Stupp, Functional supramolecular polymers, *Science*, 2012, **335**, 813–817.

4 L. Zhang, T. Wang, Z. Shen and M. Liu, Chiral nanoarchitectonics: towards the design, self–assembly, and function of nanoscale chiral twists and helices, *Adv. Mater.*, 2016, **28**, 1044–1059.

5 J. H. Lee, S. Fujii, R. Takahashi and K. Sakurai, Monodisperse micelles with aggregation numbers related to platonic solids, *Macromol. Rapid Commun.*, 2020, **41**, 2000227.

6 S. A. Lim, S. H. Jung and J. H. Jung, Kinetically controlled chiral metal–coordinated supramolecular polymerization accompanying helical inversion or morphological transformation, *Bull. Korean Chem. Soc.*, 2023, **44**, 322–331.

7 I. Park, R. Medishetty, J. Kim, S. S. Lee and J. J. Vittal, Distortional supramolecular isomers of polyrotaxane coordination polymers: photoreactivity and sensing of nitro compounds, *Angew. Chem.*, 2014, **126**, 5697–5701.

8 S. H. Jung, K. Y. Kwon and J. H. Jung, A turn-on fluorogenic Zn(II) chemoprobe based on a terpyridine derivative with aggregation-induced emission (AIE) effects through nanofiber aggregation into spherical aggregates, *Chem. Commun.*, 2015, **51**, 952–955.

9 E. Lee, H. Ju, I.-H. Park, J. H. Jung, M. Ikeda, S. Kuwahara, Y. Habata and S. S. Lee, Pseudo[1]catenane-type pillar[5] thiacrown whose planar chiral Inversion is triggered by metal cation and controlled by anion, *J. Am. Chem. Soc.*, 2018, **140**, 9669–9677.

10 S. Lee, K. Y. Kim, S. H. Jung, J. H. Lee, M. Yamada, R. Sethy, T. Kawai and J. H. Jung, Finely controlled circularly polarized luminescence of a mechano-responsive supramolecular polymer, *Angew. Chem., Int. Ed.*, 2019, **58**, 18878–18882.

11 C. Zhu, Y. Mu, Y. Li, K. Y. Wang, X. Ma, S. Tu, Y. Fu, L. Cheng, X. Wu and Y. Li, Polypeptide-inspired supramolecular assemblies for enantioselective sorption of chiral molecules, *Inorg. Chem. Front.*, 2024, **11**, 1492–1500.

12 K. L. Gurunatha and E. Dujardin, Tuning the optical coupling between molecular dyes and metal nanoparticles by the templated silica mineralization of J-aggregates, *J. Phys. Chem. C*, 2013, **117**, 3489–3496.

13 S. H. Jung, J. Jeon, H. Kim, J. Jaworski and J. H. Jung, Chiral arrangement of achiral Au nanoparticles by supramolecular assembly of helical nanofiber templates, *J. Am. Chem. Soc.*, 2014, **136**, 6446–6452.

14 X. Lan, X. Lu, C. Shen, Y. Ke, W. Ni and Q. Wang, Au nanorod helical superstructures with designed chirality, *J. Am. Chem. Soc.*, 2015, **137**, 457–462.

15 A. D. Merg, J. C. Boatz, A. Mandal, G. Zhao, S. Mokashi-Punekar, C. Liu, X. Wang, P. Zhang, P. C. A. van der Wel and N. L. Rosi, Peptide-directed assembly of single-helical gold nanoparticle superstructures exhibiting intense chiroptical activity, *J. Am. Chem. Soc.*, 2016, **138**, 13655–13663.

16 Y. Shi, P. Duan, S. Huo, Y. Li and M. Liu, Endowing perovskite nanocrystals with circularly polarized luminescence, *Adv. Mater.*, 2018, **30**, 1705011.

17 L. Chen, J. Zheng, J. Feng, Q. Qian and Y. Zhou, Reversible modulation of plasmonic chiral signals of achiral gold nanorods using a chiral supramolecular template, *Chem. Commun.*, 2019, **55**, 11378–11381.

18 D. Vila-Liarte, N. A. Kotov and L. M. Liz-Marzán, Template-assisted self-assembly of achiral plasmonic nanoparticles into chiral structures, *Chem. Sci.*, 2022, **13**, 595–610.

19 D. Chakraborty, A. Akhuli, N. Preeyanka and M. Sarkar, Energy-transfer-induced enhanced valley splitting of excitonic emission of inorganic CdTe@ZnS QDs in the presence of organic J-aggregates: a spectroscopic insight into the efficient exciton (inorganic)-exciton (organic) coupling, *J. Phys. Chem. C*, 2023, **127**, 5082–5089.

20 Y. Tu, F. Peng, A. Adawy, Y. Men, L. K. E. A. Abdelmohsen and D. A. Wilson, Mimicking the cell: bio-inspired functions of supramolecular assemblies, *Chem. Rev.*, 2015, **116**, 2023–2078.

21 S. Mohnani and D. Bonifazi, Supramolecular architectures of porphyrins on surfaces: The structural evolution from 1D to 2D to 3D to devices, *Coord. Chem. Rev.*, 2010, **254**, 2342–2362.

22 A. Sorrenti, Z. El-Hachemi, O. Arteaga, A. Canillas, J. Crusats and J. M. Ribo, Kinetic control of the supramolecular chirality of porphyrin J-aggregates, *Chem. – Eur. J.*, 2012, **18**, 8820–8826.

23 T. Hasobe, Porphyrin-based supramolecular nanoarchitectures for solar energy conversion, *J. Phys. Chem. Lett.*, 2013, **4**, 1771–1780.

24 S. Durot, J. Taesch and V. Heitz, Multiporphyrinic cages: architectures and functions, *Chem. Rev.*, 2014, **114**, 8542–8578.

25 R. Zagami, M. A. Castriciano, A. Romeo, M. Trapani, R. Pedicini and L. M. Scolaro, Tuning supramolecular chirality in nano and mesoscopic porphyrin J-aggregates, *Dyes Pigm.*, 2017, **142**, 255–261.

26 N. Keller, M. Calik, D. Sharapa, H. R. Soni, P. M. Zehetmaier, S. Rager, F. Auras, A. C. Jakowetz, A. Görling, T. Clark and T. Bein, Enforcing extended porphyrin J-aggregate stacking in covalent organic frameworks, *J. Am. Chem. Soc.*, 2018, **140**, 16544–16552.

27 R. Randazzo, M. Gaeta, C. M. A. Gangemi, M. E. Fragalà, R. Purrello and A. D'Urso, Chiral recognition of L- and D-amino acid by porphyrin supramolecular aggregates, *Molecules*, 2019, **24**, 84.

28 G. Magna, D. Monti, C. D. Natale, R. Paolesse and M. Stefanelli, The assembly of porphyrin systems in well-defined nanostructures: an update, *Molecules*, 2019, **24**, 4307.

29 Y. Keum, B. Kim, A. Byun and J. Park, Synthesis and photocatalytic properties of titanium-porphyrinic aerogels, *Angew. Chem.*, 2020, **132**, 21775–21780.

30 M. Stefanelli, F. Mandoj, G. Magna, R. Lettieri, M. Venanzi, R. Paolesse and D. Monti, The self-aggregation of porphyrins with multiple chiral centers in organic/aqueous media: the case of sugar- and steroid-porphyrin conjugates, *Molecules*, 2020, **25**, 4544.

31 N. K. Shee and H. J. Kim, Morphology-controlled self-assembled nanostructures of complementary metalloporphyrin triads obtained through tuning their intermolecular coordination and their photocatalytic degradation of Orange II dye, *Inorg. Chem. Front.*, 2022, **10**, 174–183.

32 N. Sasaki, J. Kikkawa, Y. Ishii, T. Uchihashi, H. Imamura, M. Takeuchi and K. Sugiyasu, Multistep, site-selective non-covalent synthesis of two-dimensional block supramolecular polymers, *Nat. Chem.*, 2023, **15**, 922–929.

33 M. S. L. Mendes, G. Duroux, A. Boudier, P. Pranee, Y. Okazaki, T. Buffeteau, S. Massip, S. Nlate, R. Oda, E. Hillard and E. Pouget, Porphyrin J-aggregates as a probe for chiral impurities as demonstrated by their symmetry breaking by confinement in montmorillonite clay, *Nanoscale*, 2025, **17**, 1334–1341.

34 Y. Rong, P. Chen and M. Liu, Self-assembly of water-soluble TPPS in organic solvents: from nanofibers to mirror imaged chiral nanorods, *Chem. Commun.*, 2013, **49**, 10498–10500.

35 H. Jiang, L. Zhang, J. Chen and M. Liu, Hierarchical self-assembly of a porphyrin into chiral macroscopic flowers with superhydrophobic and enantioselective property, *ACS Nano*, 2017, **11**, 12453–12460.

36 Y. Kitagawa, H. Segawa and K. Ishii, Magneto-chiral dichroism of organic compounds, *Angew. Chem., Int. Ed.*, 2011, **50**, 9133–9136.

37 M. Shirakawa, S. Kawano, N. Fujita, K. Sada and S. Shinkai, Hydrogen-bond-assisted control of H versus J aggregation mode of porphyrins stacks in an organogel system, *J. Org. Chem.*, 2003, **68**, 5037–5044.

38 G. A. Hembury, V. V. Borovkov and Y. Inoue, Chirality-sensing supramolecular systems, *Chem. Rev.*, 2008, **108**, 1–73.

39 I. G. Occhiuto, M. A. Castriciano, M. Trapani, R. Zagami, A. Romeo, R. F. Pasternack and L. M. Scolaro, Controlling J-aggregates formation and chirality induction through demetallation of a zinc(II) water soluble porphyrin, *Int. J. Mol. Sci.*, 2020, **21**, 4001.

40 I. G. Occhiuto, R. Zagami, M. Trapani, M. A. Castriciano, A. Romeo and L. M. Scolaro, Kinetic investigation on tetrakis(4-sulfonatophenyl)porphyrin J-aggregates formation catalyzed by cationic metallo-porphyrins, *Molecules*, 2020, **25**, 5742.

41 A. Adawy, Functional chirality: from small molecules to supramolecular assemblies, *Symmetry*, 2022, **14**, 292.

42 W. K. Bae, J. Kwak, J. W. Park, K. Char, C. Lee and S. Lee, Highly efficient green-light-emitting diodes based on CdSe@ZnS quantum dots with a chemical-composition gradient, *Adv. Mater.*, 2009, **21**, 1690–1694.

43 J. Lee, C. Bae, Z. Ou, S. Park, J. Kim and J. Kim, Nanoscopic morphological effect on the optical properties of polymer-grafted gold polyhedra, *Nanoscale Adv.*, 2021, **3**, 1927–1933.